CWP-577

Broadside imaging of the San Andreas fault system at depth

I. Vasconcelos, R. Snieder*, S. T. Taylor†, J. A. Chavarria‡, & P. Sava*

* *Center for Wave Phenomena, Department of Geophysics, Colorado School of Mines, Golden, CO 80401, USA*
† *Earth and Ocean Sciences Division, Duke University, Durham, NC 27708, USA*
‡ *Paulsson Geophysical Services, Inc., Brea, CA 92821*

ABSTRACT

The San Andreas Fault Observatory at Depth provides perhaps the most comprehensive set of data on the structure and dynamics of the San Andreas fault. We use two independent experiments recorded by the seismometer arrays of the SAFOD Pilot and Main Holes to resolve the localized structure of the San Andreas fault zone and of an intermediate fault zone at depth. From Pilot Hole recordings of the drilling noise coming from the Main Hole, we reconstruct the waves that propagate between the Pilot Hole sensors and use them to image the fault zone structure. The use of correlated drilling noise leads to a high-resolution image of a major transform fault zone. Another independent image is generated from the detonation of a surface explosive charge recorded at a large 178-sensor array placed in the Main Hole. The images reveal the San Andreas fault as well as an active blind fault zone that could potentially rupture. This is confirmed by two independent methods. The structure and the activity of the imaged faults is of critical importance to understanding the current stress state and activity of the San Andreas fault system.

Key words: San Andreas Fault, VSP, seismic-while-drilling, deconvolution interferometry, reverse-time migration

1 THE SAFOD PROJECT

The San Andreas Fault Observatory at Depth (SAFOD) was conceived to closely study and monitor the earthquake dynamics and structure of the San Andreas Fault (SAF) at Parkfield, CA (http://www.icdp-online.de/sites/sanandreas/index/index.html). Characterizing the structure and dynamics of the SAF strike-slip system is crucial for understanding the geodynamics of transform plate boundaries and their associated seismicity. In particular, the SAF at Parkfield has historically been seismically active, with seven catalogued earthquakes of magnitude six approximately (Bakun and McEvilly, 1984; Roeloffs and Langbein, 1994); the latest one occurred in September 2004 (Kerr, 2006).

Consisting of a vertical borehole, the Pilot Hole (PH), and of a deviated well that intersects the SAF, the Main Hole (MH), SAFOD is designed to sample and monitor the SAF system from within the subsurface at Parkfield. Together with surface observations, data from SAFOD already contributed greatly to the understanding of the SAF system at Parkfield. Figure 1a is a scaled schematic cartoon that summarizes and connects results from several publications that analyze data from the SAFOD site. Much of the information on the surface geology and on the basement and sedimentary structures at Parkfield comes from geologic mapping (Rymer et al., 2003) and from surface refraction (Catchings et al., 2003) and reflection (Hole et al., 2001; Catchings et al., 2003) seismic data. The lateral delineation of the Salinian granite to the SW of the SAF has also been inferred from magnetotelluric (Unsworth et al., 2000; Unsworth and Bedrosian, 2004) measurements and from joint inversion of gravity and surface seismic data (Figure 1b; Roecker et al., 2004; and Thurber et al., 2004).

Analysis of PH rock samples (Solum et al., 2004) and of their in-situ physical properties (Boness and Zoback, 2004) helped determine the lithology and the stress state around the PH. Likewise, recent studies of rock samples from drilling (Solum et al., 2006) and well-logs (Boness and Zoback, 2006) from the MH have shed light on the subsurface geology along the SAFOD MH. It was not until 2006 that the SAFOD MH first intersected the SAF (Figure 1a), and the upcoming coring of the SAF system during the Phase 3 drilling of the MH (summer 2007) promises to bring important information on the internal composition of the SAF.

Previous to the drilling of the SAFOD MH, microseismic events along with surface active-shots recorded at the PH seismometer array were used to make some of the first images of the SAF at depth (Chavarria et al., 2003) which also contributed much to our understanding of the subsurface geology at Parkfield (Figure 1a). As a continuation of the subsurface imaging at Parkfield, we use drilling noise recorded at the PH and an active-shot experiment recorded at the SAFOD MH to obtain high-resolution images of the SAF system between depths of 0 to approximately 1.5 km (from sea level; this corresponds to approximately 0.6 to 2.1 km from the surface). These images help to resolve the wave-scattering structures associated to the SAF as well as at least one other heavily faulted zone between the SAFOD drilling site and the SAF. Images such as the ones we present here are critical for the development of detailed models of the SAF plate and earthquake dynamics.

2 IMAGING THE SAF FROM PASSIVE AND ACTIVE SEISMIC DATA

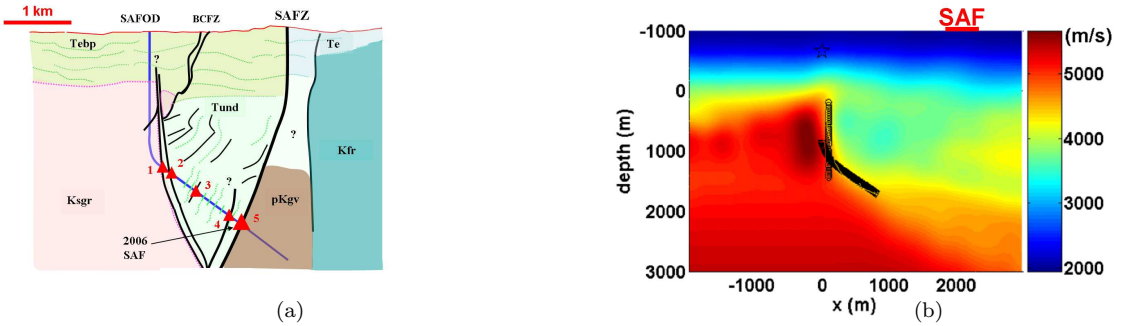
The SAFOD data we use were acquired in two experiments. The first experiment was carried out in July 2004, when the SAFOD PH receiver array (Figure 1b) was switched on to constantly monitor the drilling noise during the early stages of the drilling of the SAFOD MH. We used the drill-bit noise recordings of the SAFOD PH array to create an image of the SAF. In a second independent experiment, conducted in 2005, a large 178-receiver array was placed in the SAFOD MH (Figure 1b) to record the active shooting of an 80-pound explosive charge placed at the surface near the SAFOD MH. We also used this shot record to image the SAF. These two experiments differ not only on the geometry of the data acquisition (i.e., source and receiver positioning), but also in the physical character of the excitation that generates the recorded waves. To account for the differences between the PH and the MH data, we applied different processing to each dataset and to subsequently produce the images. Figure 2 provides schematic representations of the data acquisition geometry for the PH drill-bit noise recordings and for the MH active-shot experiment.

To create an image of the SAF zone from the drill-bit noise records we rely on the concept of seismic interferometry (Curtis et al., 2006; Larose et al., 2006). Interferometry recovers the response between any two receivers in an arbitrarily heterogeneous and anisotropic medium as if a source was placed at one of the receiver locations(Lobkis and Weaver, 2001; Snieder et al., 2006). We only briefly highlight the issues of interferometry that are of particular concern to the processing of the SAFOD PH drilling noise records.

Typically, interferometry makes use of cross-correlations between recorded data to recover waves propagating between receivers (Lobkis and Weaver, 2001). By doing so, the recovered receiver response includes an average of the power spectra of the excitations(Lobkis and Weaver, 2001, Snieder et al., 2006). Removing the contribution of the source power spectrum is an issue when recovering signals from drill-bit noise because in this case the wave-generation mechanism is constantly active, and the spectrum is heavily dominated by specific vibration modes associated to the drilling process (Poletto and Miranda, 2004). An example of this behavior from SAFOD PH-array records can be found in Figure 4a.

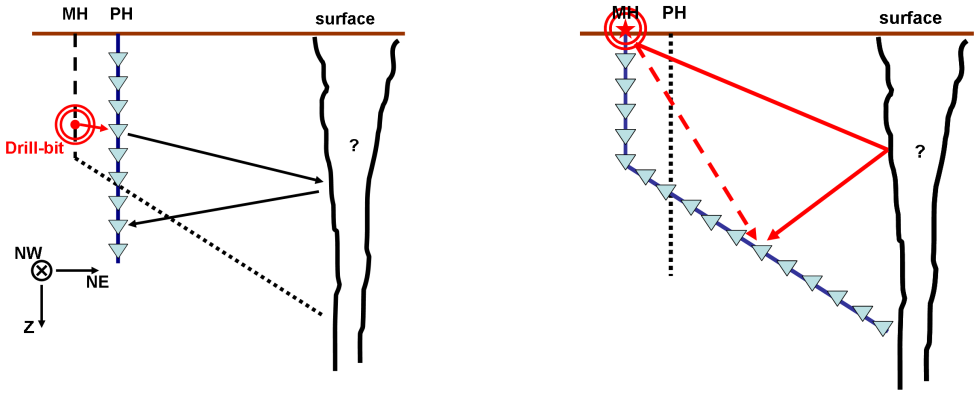
It is possible, however, to remove the drill-bit source signature from drilling noise records (Poletto and Miranda, 2004). The standard industry practice is to estimate the drill-bit signature by placing accelerometers on the drill-stem (Poletto and Miranda, 2004; Rector and Marion, 1991). This estimate is then used to extract the drill-bit noise signature from the cross-correlations of the recorded data, leaving only the approximate impulse response of the Earth (Lobkis and Weaver, 2001; Poletto and Miranda, 2004). Following this accelerometer-based approach, drill-bit imaging has been previously applied to surface recordings of MH drilling noise at Parkfield (Taylor et al., 2005). In our case, such accelerometer recordings are not available. As an alternative to interferometry by cross-correlations, we used an interferometry technique based on deconvolutions (Vasconcelos and Snieder, 2007). This technique synthesizes the response between receivers from incoherent excitations as if one of the receivers acted as a pseudo-source, while canceling the effect of the drill-bit source signature without the need for drill-stem accelerometers.

In Figure 3a we show the result from processing approximately 17 hours of drilling noise records into a shot record with a pseudo-source at receiver PH-26. With the pseudo-source centered at 0 s, PH-26 acts as the pseudo-shot responsible for the excitation of waves (Vasconcelos and Snieder, 2007). Figure 3a shows the direct wave that propagates from receiver PH-26 and is recorded at the other receivers. The reflection events highlighted in Figure 3a are caused by faults in the SAF system. The data in Figure 3a represents waves excited by a vertically-oriented force (see Figure 4). In addition, we are also able to recover the excitation at receiver PH-26



(a) (b)

Figure 1. Panel (a) shows our current knowledge of the structure of the San Andreas fault system at Parkfield, CA. The main geologic formations are indicated by different colors and by their corresponding acronyms, these are: the Tertiary Ethegoin (Te), Tertiary Ethegoin-Big Pappa (Tebp), Tertiary undifferentiated (Tund), Cretaceous Franciscan rocks (Kfr), Cretaceous Salinian Granite (Ksgr), and the pre-Cretaceous Great Valley (pKgv). The SAFOD main-hole (MH) is indicated by the blue solid line. Black solid lines in (a) represent faults. BCFZ refers to the Buzzard Canyon Fault zone. The areas where the finer-scale structure of the SAF system were unknown are indicated by question marks. The red triangles, numbered 1 through 5, show approximate locations of intersections of the MH with major zones of faulting (Solum et al., 2006). Triangle number 5 represents the point where the MH penetrated the SAF in 2006. Panel (b) shows the large-scale structure of the P-wave velocity field (velocities are colorcoded) that approximately corresponds to the schematic representation in (a). The circles in (b) indicate the location of the sensors of the SAFOD pilot-hole array used here for the recording of drilling noise. The SAFOD MH array, used in the active-shot experiment, is indicated by the triangles. The location of the active shot is depicted by the star. Depth is with respect to sea level, the altitude at SAFOD is of approximately −660 m.

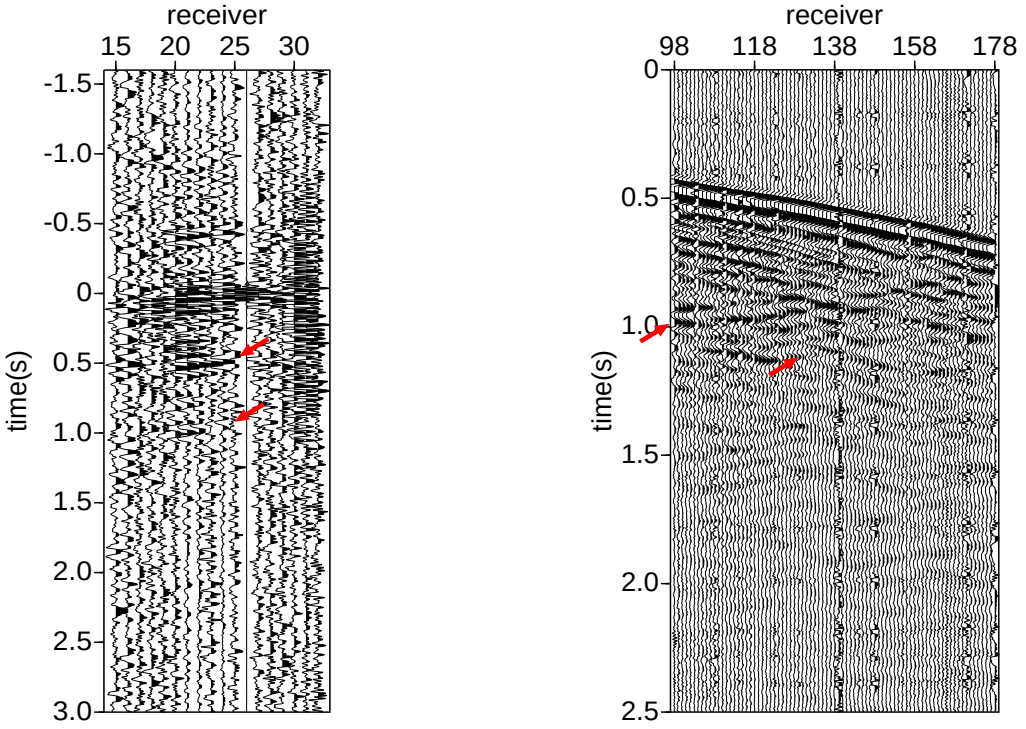


(a) (b)

Figure 2. Schematic acquisition geometries of SAFOD data. Receivers are indicated by the light-blue triangles. The structures outlined by black solid lines to the right-hand side of the figure represent a target fault. (a) shows the acquisition geometry of the downhole seismic-while-drilling (SWD) dataset. It consists of multiple 60 second-long recordings of drill-bit noise excited at different depths, recorded at 32 3-component receivers in the PH. As indicated by (a), receivers are oriented in the Z-(or downward vertical), NE- and NW-directions. (a) also shows a schematic stationary path between the drill-bit and two receivers. Interferometry recovers only the portion of the propagation path represented by black arrows in (a). The active-shot geometry in (b) is comprised of 178 3-component receivers placed in the MH. The dashed red arrow in (b) represents all waves that propagate towards the NE (right-hand side of the figure), while the solid red line represents all waves going toward SW (left-hand side of (b)). The inclination of the deviated portion of the MH is of about 45° with respect to the vertical. The receiver components of the SAFOD MH array are co-oriented with those of the PH array, whose orientations are shown in (a).

associated to a Northeast-oriented force (see Figure 4c). The SAFOD interferometric image we will discuss here is a product from imaging the pseudo-shots at PH-26 excited by forces oriented both in the vertical and in the Northeast (NE) directions.

Unfortunately, out of almost two months of recording drilling noise at the PH array, only about a day and a half of the data is useable for interferometry purposes due to data acquisition problems. Within this time window, the drill-bit is closest to receiver PH-26 (the dis-



(a) (b)

Figure 3. (a) Vertical component of the interferometric shot gather for a pseudo-shot position at pilot-hole receiver PH-26. Red arrows indicate reflections of interest. The reflection event that arrives at approximately 1.0 s at receiver PH-24 is interpreted to correspond to a P-wave reflection from the SAF zone. Due to the noise levels, only a subset of the 32 receivers of the PH array is sensitive to the incoming signals from the SAF zone. (b) Data recorded by the vertical component of motion in the SAFOD MH array from the active-shot experiment. The red arrows indicate two left-sloping events that are associated to P-wave reflections from faults within the SAF system.

tance between the MH and PH at that depth is of only a few meters). It is at this drill-bit position that we find the most prominent contribution from the waves excited by the drill-bit for the reconstruction of the waves that propagate between receiver PH-26 and the remaining receivers. We refer to this point as a stationary position for the drill-bit source (Snieder et al., 2006). To recover signals propagating between receivers, it is necessary to have physical sources at the stationary points that link a pair of receivers to a target reflector (Snieder et al., 2006). The only drill-bit stationary point sampled within the good-quality PH records recovers waves that emanate from receiver PH-26. This restriction limits the area of the SAF zone from which we can produce a physically meaningful image to the area shown in Figure 6a.

The shot gather from the SAFOD MH active-shot experiment (Figure 3b) shows a reflection as a left-sloping event arriving at main-hole receiver MH-98 at approximately 1.0 s (indicated by the top-most arrow). Another weaker left-sloping event that arrives at approximately 1.2 s at receiver MH-98 (lower-most arrow) is associated with a P-wave reflection from the SAF zone. Since the receivers MH-98 to MH-178 are in the deviated, deeper-most portion of the SAFOD MH (see Figure 1b), right-sloping events are mostly associated with right-going waves, whereas left-sloping events are associated with left-going waves (see also Figure 2b). This observation only holds for a subset of the receivers of the large 178-receiver MH array: the ones which lie in the deviated portion of the MH. These would be receivers MH-98 through MH-178 (Figure 3b), whose locations are shown in Figure 1b. For the purpose of imaging the SAF system from the MH array, it is important to discern between right- and left-going waves in the data because fault reflection information for this acquisition geometry is predominantly contained in left-going waves. With frequency-wavenumber filtering (Biondi, 2006), we extract only the left-sloping events from Figure 3b. We use only these events to image the SAF zone.

The process of mapping data such as in Figure 3

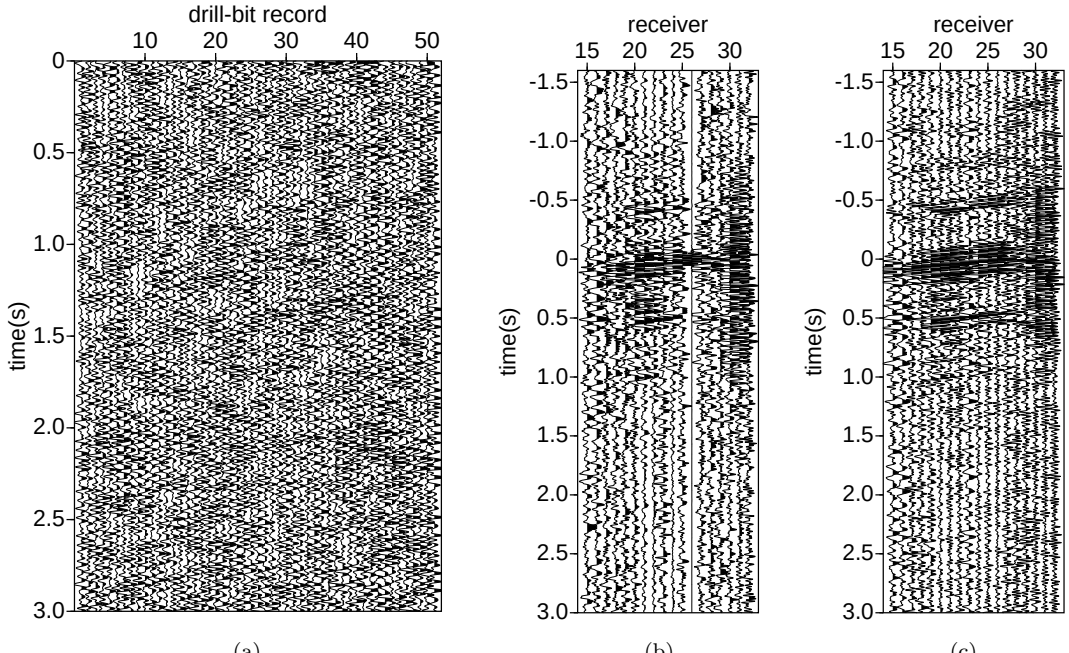


Figure 4. (a) Short samples of sequential recordings of drilling noise from the receiver PH-26. The visually monochromatic character of the records is due to drilling vibrational modes. (b) Vertical component of the interferometric shot gather for a pseudo-shot position at pilot-hole receiver PH-26. The recording at (b) represents waves excited by a vertical point-force. (c) is also the vertical component for a pseudo-shot at PH-26, but unlike the wavefield in (b), it represents waves excited by a point-force in the NE-direction. The complicated character of the drilling noise in (a) is attenuated by the interferometry procedure that produces the data in (b) and in (c). Note that receiver PH-32 is the shallowest receiver in the SAFOD PH array (see Figure 1b in main text).

into a subsurface image (Figure 6) is what we refer to as *imaging* or *migration*. Imaging typically requires a velocity model of the subsurface; the one we use is shown in Figure 1b. This model was estimated from surface seismic tomography (Thurber et al., 2004). We do the imaging of the PH and MH data (Figure 3) with two different methodologies. For imaging from the PH data we use the technique of shot-profile migration by wavefield extrapolation (Biondi, 2006). The wavefield extrapolation is done by the split-step fourier phase-shift plus interpolation method. The MH active-shot data in Figure 3b is imaged by *reverse-time migration* (Biondi, 2006).

3 HIGH-RESOLUTION IMAGES AND THE SAF

The images from the SAFOD PH and MH arrays are shown in Figures 6a and b (also in Figures S3a and b). The interferometric image from PH array (Figures 6a and S3a) provides a different area of "illumination" of the subsurface than the active-shot image from the MH array (Figures 6b and S3b). This is a consequence of the differences in the acquisition geometry of these two experiments. The images displaying all subsurface positions corresponding to the velocity model in Figure 1b are shown in the support Figure 5. A numerical model was build for the MH active-shot data to aid us in understanding what is the subsurface area that could be illuminated by the active-shot experiments, as well as what would be the character of image artifacts caused by waves diffracted by the Salinian granite. From the portion of the synthetic image that showed physically meaningful reflectors we chose the area of illumination of the SAFOD MH image in Figure 6b. The support Figure 7 shows the results from the numerical modeling of the SAFOD MH active-shot data.

Since both images are built from single-shot data (a pseudo-shot in the PH interferometric data and the active-shot in the MH data), they are prone to artifacts associated with the limited illumination (Biondi, 2006). Additionally, the method of interferometry by deconvolutions may produce image artifacts (Vasconcelos and Snieder, 2007). It is thus critical to establish which reflectors in the images in Figure 6 (and in Figure 5) pertain to actual faults or interfaces in the subsurface.

We rely on two independent criteria to gain insight into which reflectors in Figure 6 (and in Figure 5) represent real faults and/or interfaces. The first criterion is based on the consistency of events between different images. Note that all of the available images were gener-

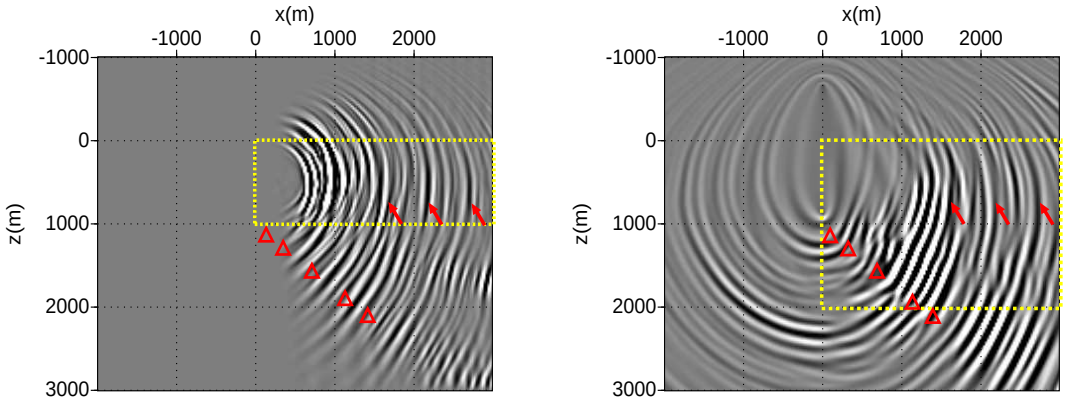


Figure 5. (a) Image obtained from stacking the results of migrating the SAFOD interferometric shot gathers in Figures S4c and d. After migrating only the left-going waves from the SAFOD MH active-shot data (Figure 2b in main text), we obtain the image in (b). The red arrows point to features that are common to both images. These features are the same as indicated by the red arrows and numbers 1 through 3 in main-text Figure 3. The dashed yellow boxes in (a) and in (b) highlight the portions of the images that are shown in main-text Figures 3a and 3b, respectively. Both yellow boxes in fact represent the subsurface area that is physically sampled by P-wave reflections, which in turn depends on the acquisition geometry of each experiment (see Figure S2). The red triangles show the approximate locations where the SAFOD MH intersected major fault zones (see main text Figure 1b). Distances in the x-axis in (a) and (b) are with respect to the location of the SAFOD drill site at the surface. The surface trace of the SAFz is at approximately $x = 2000$ m.

ated from independent experiments. In our case, on one hand we have the drilling noise recordings at the PH array, and on the other hand we have the the active-shot MH data. The images from Chavarria et al. (2003) (Figure 6) come from PH recordings of both surface active shots and microseismicity from the SAF. Not only were the data in these three experiments different, but also the corresponding images were generated by distinct methodologies. Consequently, reflectors that are consistent in two or more images are likely to be representative of actual subsurface structures.

The second criterion for interpreting reflectors in Figure 6 is the correlation between the location of fault zone intersections at the SAFOD main-hole (Solume et al., 2006) and the position of reflectors which are consistent in two or more images. The position of the five main fault zones intersected by the MH are shown schematically in Figure 1a and are superposed on the full images from the SAFOD PH and MH arrays in the support Figure 5. The comparison between MH fault intersections (Solum et al., 2006;Boness and Zoback, 2006) and reflectors in the images (Figure 5) is not always straight forward because the subsurface area illuminated by the images does not coincide with the MH well-path. Despite this difficulty, we provide our interpretation of the correlation between the MH fault intersections and imaged reflectors based on the overlay of these data (Figure 5) and on our current conceptual geologic model of the subsurface at SAFOD (Figure 1a).

In the interferometric image from the PH drilling noise records (Figure 6a) we highlight four distinct reflection events. The events 1 through 3 coincide both in the interferometric and active-shot images (Figures 6a and b, respectively; see support also Figure 5). Reflector 2 (Figure 6) is associated with the SAF, because its lateral position coincides with the lateral position of the surface trace of the SAF (marked by a vertical solid line at 0 km in the background images in Figure 6). In both the PH and MH images, the position of reflector 2 is consistent with the scattering zone associated with the SAF zone from Chavarria et al. (2003). Even though our images of the SAF (reflector 2, Figure 6) do not illuminate the fault all the way to its point of intersection with the SAFOD MH, the change in dip of the SAF in the active-shot image at approximately 1100 m depth is consistent with the intersection of the MH with fault zone 4 (Figures 1a and S3b). Since the anomaly that represents the SAF in the image by Chavarria et al. (2003) is caused by direct-wave energy coming from microseismicity within the SAF, the relative positioning between the SAF reflector in the MH active-shot image and the corresponding reflector in the background image suggests that reflector 2 may be due to P-wave energy scattered at the contact of the Franciscan rocks to the NE with the SAF zone to the SW (Solum et al., 2006; Boness and Zoback, 2006). The PH interferometric and MH active-shot images resolve structures larger than approximately 75 to 100 m in size, presenting higher resolution when compared to the previous images of the SAF at Parkfield (Hole et al., 2003; Chavarria et al.,

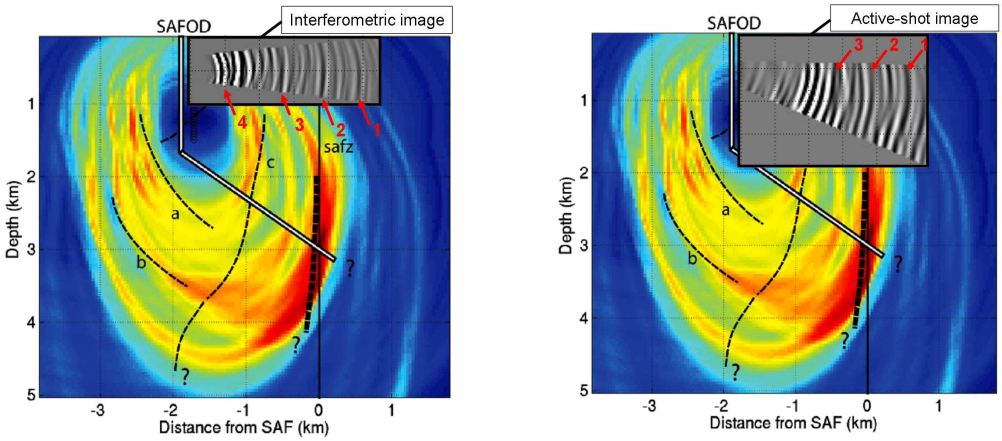


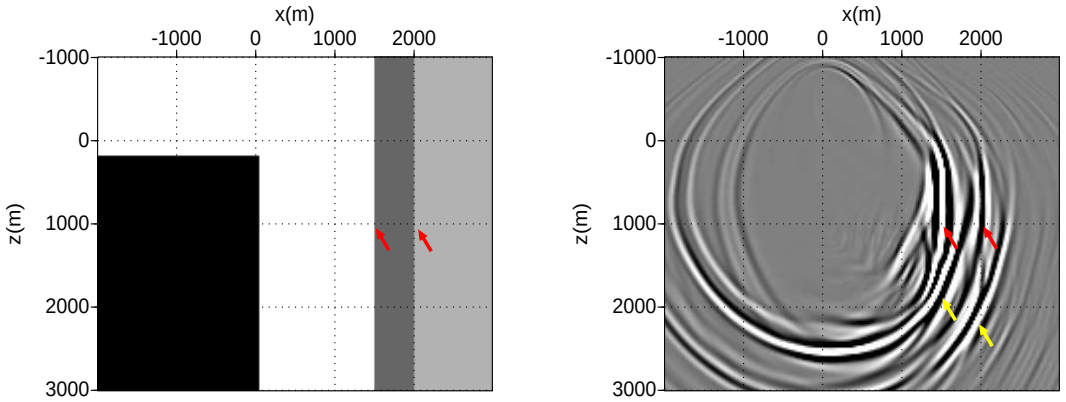
Figure 6. Images from the drill-bit noise recordings and from the active-shot experiment (in grey-scale, outlined by black-boxes). These images are overlayed on the result obtained from Chavarria et al. (2003). The overlay in (a) is the interferometric image from the SAFOD PH array, compiled after synthesizing drilling noise records into a pseudo-shot at the location of receiver PH-26. (b) shows an overlay of the image obtained from reverse-time imaging of the active-shot recorded at the SAFOD MH. The arrows mark the most prominent reflectors in the images. The reflectors numbered 1 through 3 coincide in both images. Reflectors 2 and 3, and possibly 4 are associated with fault zones. The SAF zone is visible at reflector 2 in both images. The location of the SAFOD MH in the background color images is schematic, since the MH was drilled after the work by Chavarria et al. (2003) was published. See also Figures S3a and S3b for the full images from the drill-bit noise recordings and active-shot data.

2003). The geometry of our experiments (especially of the PH drill-bit records) is ideal for the broadside imaging of the SAF, complementing the previous Parkfield experiments (Hole et al., 2003; Chavarria et al., 2003).

Although the reflector 1 is consistent between the PH interferometric image and the MH active-shot image, we do not associate it to any known faults. The reason for this is that there is no surface trace of a fault at the location of reflector 1; nor has a major fault zone yet been intersected by the SAFOD MH after the SAF. If reflector 1 is indeed an artifact produced from the imaging procedures applied to both the PH and the MH data, it was not reproduced by the numerical modeling of the SAFOD MH data. Since the modeling in Figure 7 was acoustic (accounting only for P-wave propagation), reflector 1 could be due to erroneous imaging of recorded P-to-S converted waves. Note that our imaging procedures also assume that the medium is acoustic, so any recorded converted waves will be imaged as artifact reflectors placed farther than their P-wave counterparts. This, we believe, is what happens to reflector 1; a P-to-S converted reflection perhaps related to the SAF P-wave reflector at reflector 2 (Figure 6).

The fact that reflector 4 can only be seen in the PH interferometric image is not necessarily inconsistent with the MH image because even if the reflector pertained to a physical event, its location makes it mostly invisible for the MH active-shot image (the reflector is located between the shot and most of the receivers in the MH array). The location of reflector 4 in Figure 5a suggests a possible correspondence with the SAFOD MH intersection with fault zone number 2 (Figures 1a and S3a). If such a correspondence is true, then reflector 4 is likely to represent the contrast between the Salinian granite and the sediments, which is bordered by fault zone 2 (Figure 1a).

Reflector 3 in Figure 6 is also associated with a fault zone. It is present in both the PH interferometric and in the MH active shot images, and its location coincides with the scattered energy observed by Chavarria et al. (2003) in their P-wave migration images (see Figure 3C and 3B of their paper). We associate this reflector with fault intersection number 4 (Figure 1a) in the SAFOD MH array (Solum et al., 2006; Boness and Zoback, 2006). The location of the fault intersection is close to the portion of the fault illuminated by the MH active-shot image (see Figure 5b). Also, the fault image dips in the SW direction towards the point of intersection between the SAFOD MH and fault number 4 (Figures 1a and S3b). The location of this fault zone at reflector 3 coincides with a well-resolved localized cluster of microseismic events detected both by surface records



(a) (b)

Figure 7. Acoustic numerical modeling of the SAFOD MH active-shot data. (a) shows the structure of the reflectivity model used to generate the synthetic data. The velocity model used is the same as the one used for imaging (Figure 1b in main text). The black block in the reflectivity model in (a) represents the Salinian granite (see Figure 1a in main text), whereas the grey structures to the left of the model generate two vertical fault-like features. After applying the same imaging procedure as for the field SAFOD MH data (Figure 5), we end up with the image in (b). The red arrows mark the position of the target reflectors both in the model (a) and in the image (b). The reflections of waves generated by the diffraction of energy in the corner of the granite block appear as image artifacts (marked by yellow arrows). Without the numerical model, these artifacts could potentially be misinterpreted as dipping fault structures. The objective of the numerical modeling is not to closely replicate all features of the data (Figure 2b in main text). Instead, the objective of the model is two-fold: it helps us understand which portion of the subsurface is "illuminated" by P-wave reflections in the active-shot experiment, and it gives us an idea of how P-waves that are diffracted and/or guided by the granite structure may appear in the image.

(Nadeau et al., 2004) and by the PH array (Oye et al., 2004). The images in Figure 6 show considerably higher resolution than the previous images from Chavarria et al. (2003) in imaging the intermediate fault zone corresponding to fault number 4 (Figure 1a). The imaging of this intermediate fault zone (and its subsequent intersection at the SAFOD PH) is important to the understanding of the structure of the SAF system, especially because there is no trace of this fault system at the surface. Since it is a blind fault (Yeats and Hutfile, 1995; Talebian et al., 2004), determining the activity status of fault 3 is critical in assessing its seismogenic risk. The existence of this feature interpreted from two independent observations provides the basis for a better fault zone understanding and its hazard assessment. Unknown blind faults have been the cause of major fatal earthquakes, such as the 1994 Northridge earthquake (Yeats and Hutfile, 1995) and the 2003 Bam earthquake in Iran (Talebian et al., 2004).

The dip of the SAF reflector and of the intermediate fault reflector support the interpretation of the SAF system being structurally characterized by a flower structure (Figure 1a). Previous surface seismic profiling also suggested the presence of intermediate fault zones (Hole et al., 2001) such as the one confirmed here. It remains to be understood whether this intermediate faulting is associated with the same flower structure as the SAF, potentially representing an earlier trace or an active branch of the SAF, or if these secondary faults belong to a separate flower structure (Chavarria et al., 2003). According to Solum et al. (2006), well casing deformation was only observed at fault intersection 5 (associated to the SAF, Figure 1a). The other four fault zones showed no signs of fault activity since so far there was no casing deformation associated to them. If the imaged intermediate fault zone (reflector 3, Figure 6) is indeed an inactive fault zone, it might well represent an earlier trace of the SAF. On the other hand, the clusters of microseismic activity previously observed (Nadeau et al., 2004; Oye et al., 2004) are likely associated to the imaged blind fault zone (reflector 3, Figure 6), which suggests that this fault zone is likely to be an active part of the current SAF system.

Other important factors for understanding fault activity and seismogenic potential are fault zone mineralogy, fluid content and pore-pressure. It has been previously suggested that there may be high-pressured fluids within the SAF zone at Parkfield (Unsworth et al., 2000; Unsworth and Bedrosian, 2004; Chavarria et al., 2003). Both the SAF reflector and reflector 3 in Figure 6 are consistent with the lateral positioning of the known low resistivity anomaly inferred by magnetotelluric soundings at Parkfield (Unsworth et al., 2000; Unsworth and Bedrosian, 2004). Indeed, the analysis of the inferred fault material from the SAF and from the imaged intermediate fault zone (Solum et al., 2006) shows a high

concentration of clay minerals, which are typically associated with low resistivity materials and with fluid-rich rocks. Furthermore, the analysis of rocks from the deeper SAF Solum et al. (2006) also showed the presence of serpentine, a mineral that could potentially generate fluid seals within the SAF leading to the creation of high-pressured fluid pockets inside the fault (Unsworth et al., 2000; Unsworth and Bedrosian, 2004). From the available seismic data, it is not yet possible to determine if the observed fault reflections are caused by fault-trapped fluids, by the contrast in material properties across the faults (Solum et al., 2006) or by a combination of these factors.

Nonetheless, the understanding of the structure of the SAF system has gained much from the imaging from the PH drill-bit noise and the MH active-shot experiments conducted at SAFOD. Our current images from these experiments not only provide better resolution in the structural definition of the faults within the SAF, but were also played a decisive role in the characterization of a blind fault zone between the SAFOD PH and the SAF. The high-resolution structural characterization of the SAF system is critical to the understanding of fault-growth and earthquake mechanics at Parkfield. The results we present here prove that imaging from noise can be crucial for illuminating complex fault zones in areas where observations from active experiments are insufficient. With the help of further continuous coring and analysis of fault material from the SAFOD MH Phase 3 drilling (to be conducted Summer 2007), the nature of the observed fault reflections will be perhaps better understood.

4 ACKNOWLEDGEMENTS

This research was supported through grant EAS-0609595 of the NSF. We also acknowledge the partial support of the sponsors of the Seismic Inverse Methods for Complex Structures consortium at the Center for Wave Phenomena, Colorado School of Mines. Schlumberger donated the equipment and funds for the acquisition of PH drill-bit data. Paulsson Geophysical Services, Inc. (P/GSI), acquired and donated the MH active-shot data. We thank Peter Malin (Duke University) for intermediating the data exchange, and for providing the orientation of the Pilot Hole receivers.

REFERENCES

W.H. Bakun and T.V. McEvilly. Recurrence models and Parkfield, California earthquakes. *J. Geoph. Res.*, 89:3051–3058, 1984.

B. Biondi. 3D Seismic Imaging. *Investigations in Geophysics, 14, Society of Exploration Geophysicists*, 240 pages, 2006.

N.L. Boness and M.D. Zoback. Stress-induced seismic velocity anisotropy and physical properties in the SAFOD Pilot Hole in Parkfield, CA. *Geophys. Res. Let.*, 31:L15S17, 2004.

N.L. Boness and M.D. Zoback. A multiscale study of the mechanisms controlling shear velocity anisotropy in the San Andreas Fault Observatory at Depth. *Geophysics*, 71:F131–F146, 2006.

R.D. Catchings, M.R. Goldman, M.J. Rymer, G. Gandhok, and G.S. Fuis. Data Report for the Main Line of the PSINE Seismic Survey Across the San Andreas Fault and the SAFOD Site Near Parkfield, California. *USGS Open-file Report*, 03-04:30, 2003.

R.D. Catchings, M.J. Rymer, and M.R. Goldman. Subsurface Structure of the San Andreas Fault Zone Near SAFOD From High-resolution Seismic Images. *Geophys. Res. Abs.*, 5:07861, 2003.

J.A. Chavarria, P. Malin, R.D. Catchings and E. Shalev. A look inside the San Andreas fault at Parkfield through vertical seismic profiling. *Science*, 302:1746–1748, 2003.

A. Curtis, P. Gerstoft, H. Sato, R. Snieder and K. Wapenaar. Seismic interferometry - turning noise into signal. *The Leading Edge*, 25:1082–1092, 2006.

J.A. Hole, R.D. Catchings, K.C. St. Clair, M.J. Rymer, D. A. Okaya, and B. J. Carney. Steep-Dip Seismic Imaging of the Shallow San Andreas Fault Near Parkfield *Science*, 294:1513–1515, 2001.

R. A. Kerr. Parkfield keeps secrets after long awaited quake. *Science*, 306:206–207, 2006.

E. Larose, L. Margerin, A. Derode, B. van Tiggelen, M Campillo, N. Shapiro, A. Paul, L. Stehly and M. Tanter. Correlation of random wavefields: An interdisciplinary review. *Geophysics*, 71:SI11-SI21, 2006.

O.I. Lobkis and R.L. Weaver. On the emergence of the Green's function in the correlations of a diffuse field. *J. Acoust. Soc. Am.*, 110:3011-3017, 2001.

R.M. Nadeau, A. Michelini, R.A. Uhrhammer, D. Dolenc and T.V. McEvilly. Detailed kinematics, structure and recurrence of micro-seismicity in the SAFOD target region. *Geophys. Res. Let.*, 31:L12S08, 2004.

V. Oye, J.A. Chavarria and P. Malin. Determining SAFOD area microearthquake locations solely with the Pilot Hole seismic array data. *Geophys. Res. Let.*, 31:L12S10, 2004.

F. Poletto and F. Miranda. Seismic while drilling, fundamentals of drill-bit seismic for exploration. *Handbook of Geophysical Exploration*, Vol 35, 2004.

J.W. Rector III and B.P. Marion. The use of drill-bit energy as a downhole seismic source. *Geophysics*, 56:628-634, 1991.

S. Roecker, C. Thurber and D. McPhee. Joint inversion of gravity and arrival time data from Parkfield: New constraints on structure and hypocenter locations near the SAFOD drill site. *Geophys. Res. Let.*, 31:L12S04, 2004.

E. Roeloffs and J. Langbein. The earthquake prediction experiment at Parkfield, California. *Reviews of Geophysics*, 32:315–336, 1994.

M.J. Rymer, R.D. Catchings and M.R. Goldman. Structure of the San Andreas fault as revealed by surface geologic mapping and high-resolution seismic profiling near Parkfield, California. *Geophys. Res. Abstr.*, 5, 13:513, 2003.

R. Snieder, K. Wapenaar and K. Larner. Spurious multiples in seismic interferometry of primaries. *Geophysics*, 71:SI111-SI124, 2006.

J.G. Solum and B.A. van der Pluijm. Phyllosilicate mineral assemblages of the SAFOD Pilot Hole and comparison with an exhumed segment of the San Andreas Fault System. *Geophys. Res. Let.*, 31:L15S19, 2004.

J.G. Solum, S.H. Hickman, D.A. Lockner, D.E. Moore, B.A. van der Pluijm, A.M. Schleicher and J.P. Evans. Mineralogical characterization of protolith and fault rocks from the SAFOD Main Hole. *Geophys. Res. Let.*, 33:L21314, 2006.

M. Talebian, E.J. Fielding, G.J. Funning, M. Ghorashi, J. Jackson, H. Nazari, B. Parsons, K. Priestley, P.A. Rosen, R. Walker, and T.J. Wright. The 2003 Bam (Iran) earthquake: Rupture of a blind strike-slip fault. *Geophys. Res. Let.*, 31:L11611, 2004.

S.T. Taylor, P. Malin, E. Shalev, J.B.U. Haldorsen, R. Coates, and C. Stolte. Drill bit seismic imaging of the San Andreas Fault System at SAFOD. *Soc. of Expl. Geophys. Exp. Abstr.*, 24:2657–2660, 2005.

C. Thurber, S. Roecker, H. Zhang, S. Baher and W. Ellsworth. Fine-scale structure of the San Andreas fault zone and location of the SAFOD target earthquakes. *Geophys. Res. Let.*, 31:L12S02, 2004.

I. Vasconcelos and R. Snieder. Interferometry by deconvolution, Part I: theory and numerical examples. *in preparation*, 2007.

M. Unsworth, P. Bedrosian, M. Eisel, G. Ebert and W. Siripunvaraporn. Along strike variations in the electrical structure of the San Andreas Fault at Parkfield, CA. *Geophys. Res. Let.*, 27:3021–3024, 2000.

M. Unsworth and P. Bedrosian. Electrical resistivity at the SAFOD site from magnetotelluric exploration. *Geophys. Res. Let.*, 31:L12S05, 2004.

R.S. Yeats and G.J. Hutfile. The Oak Ridge fault system and the 1994 Northridge earthquake. *Nature*, 373:418–420, 1995.